

# Real-time Exchange of the Lipid-bound Intermediate and Post-fusion States of the HIV-1 gp41 Ectodomain

Sai Chaitanya Chiliveri, John M. Louis, Robert B. Best and Ad Bax\*

Laboratory of Chemical Physics, National Institute of Diabetes and Digestive and Kidney Diseases, National Institutes of Health, Bethesda, MD 20892, USA

Correspondence to Ad Bax: [bax@nih.gov](mailto:bax@nih.gov) (A. Bax) @SaiChiliveri (S.C. Chiliveri), @Ad\_Bax\_4NMR (A. Bax) <https://doi.org/10.1016/j.jmb.2022.167683>

Edited by M.F. Summers

## Abstract

The envelope glycoprotein gp41 of the HIV-1 virus mediates its entry into the host cell. During this process, gp41 undergoes large conformational changes and the energy released in the remodeling events is utilized to overcome the barrier associated with fusing the viral and host membranes. Although the structural intermediates of this fusion process are attractive targets for drug development, no detailed high-resolution structural information or quantitative thermodynamic characterization are available. By measuring the dynamic equilibrium between the lipid-bound intermediate and the post-fusion six-helical bundle (6HB) states of the gp41 ectodomain in the presence of bilayer membrane mimetics, we derived both the reaction kinetics and energies associated with these two states by solution NMR spectroscopy. At equilibrium, an exchange time constant of about 12 seconds at 38 °C is observed, and the post-fusion conformation is energetically more stable than the lipid-bound state by 3.4 kcal mol<sup>-1</sup>. The temperature dependence of the kinetics indicates that the folding occurs through a high-energy transition state which may resemble a 5HB structure. The energetics and kinetics of gp41 folding in the context of membrane bilayers provide a molecular basis for an improved understanding of viral membrane fusion.

Published by Elsevier Ltd.

## Introduction

The surface-exposed envelope glycoprotein (Env or gp120/gp41) of the HIV-1 virus initiates infection by promoting fusion of the viral and host cell membranes.<sup>1,2</sup> In this process, through a sequence of large conformational changes, Env switches from its metastable pre-fusion to a lowest energy post-fusion state (Figure 1).<sup>3–7</sup> In this post-fusion state, gp41 adopts a homotrimeric 6-helix bundle (6HB), where the central coiled-coil trimer formed by heptad repeat 1 (HR1) is surrounded by three exterior HR2 helices.<sup>8</sup> The energy released during the transition from the pre- to the post-fusion state aids in surmounting the high barrier required to bring together and fuse the two negatively charged membranes.<sup>5</sup> *In vitro*, in aqueous buffer, peptides derived from HR1 and HR2 spontaneously assem-

ble to form a water-soluble 6HB structure that represents the core of the post-fusion gp41 ectodomain.<sup>8,9</sup> While several high-resolution structures for the pre- and post-fusion states of these class I fusion proteins are available across several viruses,<sup>6</sup> structural information on the intermediate states is limited due to their sparse population and transient nature.<sup>10,11</sup>

In the presence of dodecyl phosphocholine (DPC) micelles, the gp41-6HB structure, formed by the minimal polypeptide regions of HR1 and HR2, connected by a short loop (*i.e.*, N34(L6)C28;<sup>9</sup> termed Core), dissociates into monomers (Figure 1 (D)).<sup>12</sup> This observation is consistent with high membrane affinity observed for segments of the ectodomain of class I fusion proteins.<sup>13–16</sup> A similar dissociation observed for the ectodomain of Spike, the class-I fusion protein of SARS-CoV-2, supports

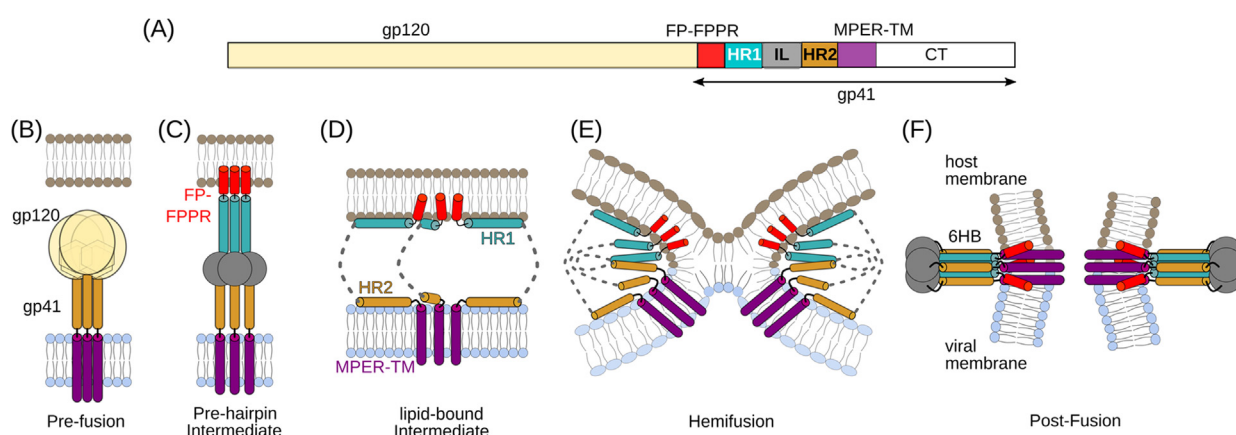


**Figure 1.** HIV-1 membrane fusion model. (A) Domain architecture of the HIV-1 envelope protein composed of subunits gp120 (light yellow) and gp41. Domain coloring for gp41: fusion peptide and fusion peptide proximal region (FP-FPPR), red; heptad repeat 1 (HR1), teal; immunodominant linker (IL), gray; heptad repeat 2 (HR2), orange; membrane proximal external region and transmembrane (MPER-TM), purple; and cytoplasmic tail, white. (B–F) Cartoon model for membrane fusion mechanism. (B) Prefusion, (C) pre-hairpin intermediate, (D) lipid-bound intermediate, (E) hemifusion, and (F) post-fusion states. Lipids of the host and viral cell membranes are colored in light brown and light blue, respectively.

the importance of the lipid-bound intermediate state (Figure 1(D)).<sup>17</sup> In the monomeric phospholipid-bound state, both HR1 and HR2 regions adopt  $\alpha$ -helical structures and lack any stabilizing interhelical tertiary interactions.<sup>18</sup> As the dissociation of 6HB in the presence of detergent micelles occurs spontaneously and is for practical purposes unidirectional, kinetics and free-energy differences associated with the 6HB to lipid-bound transition could not be obtained.

In the current study, we used membrane bilayer mimetics (bicelles),<sup>19</sup> to establish an equilibrium where both the lipid (or bicelle)-bound and 6HB states could be visualized simultaneously. The transition between the two states was found to be reversible and could be conveniently altered by varying the temperature or the concentration of protein or bicelles. This system enabled solution NMR measurement of the free energy differences and kinetics associated with these states for the wild-type HIV-1 gp41 Core and a destabilized engineered mutant of 6HB.

## Results and Discussion

Owing to its  $C_3$ -symmetry, the 6HB of gp41-Core displays a single set of resonances in a two-dimensional (2D) heteronuclear single quantum correlation (HSQC) NMR spectrum (Figure S1 (A)).<sup>12</sup> However, whereas dissociation of Core into monomers was complete upon addition of foscholine detergent,<sup>12</sup> an equilibrium between 6HB and monomeric, lipid-bound states is observed in the presence of phospholipid [ $q \sim 0.5$ , *i.e.*, 1:2 molar ratio of 1,2-dimyristoyl-*sn*-glycero-3-phosphocholine (DMPC)/ 1,2-dihexanoyl-*sn*-

glycero-3-phosphocholine (DHPC)] bicelles (Figure S1(B)), where a single bicelle contains a total of *ca* 100 DMPC and DHPC molecules. Consequently, the HSQC spectrum reveals two sets of resonances for the Core in the presence of bicelles, indicative of slow exchange on the NMR chemical shift time scale between the lipid-bound and 6HB conformers (Figure 2 and Figure S1(B)). Further, small changes in chemical shifts of up to 0.015 ppm for the 6HB state in the presence of bicelles suggest weak transient interactions between 6HB and bicelles, and the very small values of the chemical shift changes when titrating in bicelles indicate that the 6HB population predominantly (>98%) remains in the bicelle-unbound state (Figure S2(A)–(C)). The mechanism for dissociation of 6HB into lipid-bound monomers involves a coupled reaction of trimer dissociation into monomers and lipid-monomer association. However, free monomer species are not observed in the NMR spectrum, limiting information on the above two processes. As we observe two sets of resonances, one corresponding to a major bicelle-unbound 6HB state and the other, a bicelle bound monomer, the reaction mechanism is simplified as the 6HB trimer interacting with bicelles to result in a bicelle-bound monomer (Eq. (1)). A titration series of the Core by varying concentrations of lipids shows that the monomer:trimer ratio,  $[M]^3/[T]$ , scales approximately with the square of the bicelle concentration, suggesting that interaction of 6HB with two bicelles is required for the 6HB dissociation (Figure S2(D)). Presumably, this process then reflects binding of a second bicelle to the small population of transiently formed near-native 6HB:bicelle complex, and may mimic the transition of the ectodomain structure when fusing the two apposed membranes. We note

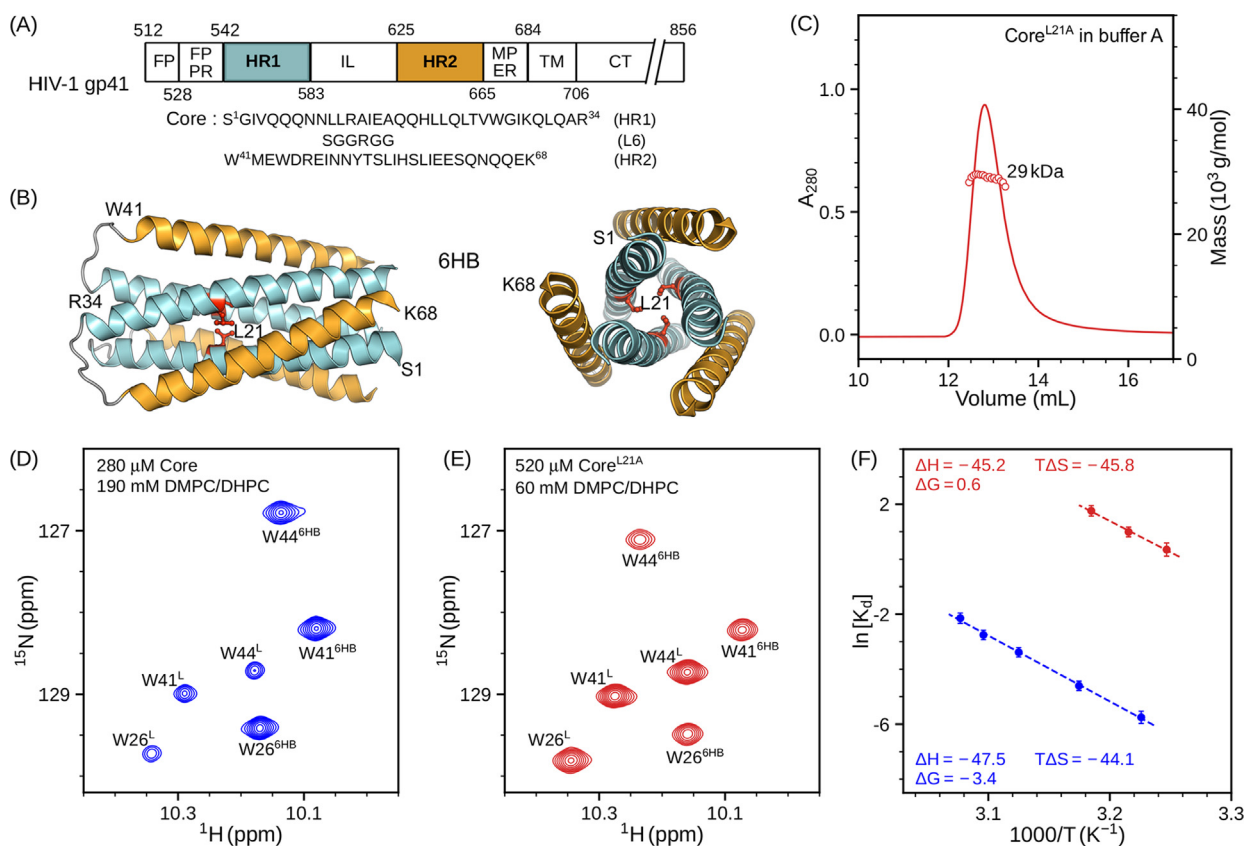


**Figure 2.** Visualization of post-fusion and lipid-bound states of HIV-1 gp41 Core. (A) Domain architecture of gp41 with domain boundaries and sequence numbering for the Core construct, comprising amino acids from HR1 and HR2 domains. (B) Ribbon representation of the 6HB (post-fusion) structure (PDB ID: 1S7T) of Core. HR1 and HR2 helices are shown in teal and orange, respectively, and the L21 sidechain in red. (C) UV absorbance profile (red solid line) for Core<sup>L21A</sup> at 280 nm fractionated on a 1 × 30 cm Superdex-75 column in buffer A at room temperature. An estimate of 29 kDa (at 25 μM peak apex concentration) by SEC-MALS (open circles) corresponds to trimer. Small regions from <sup>1</sup>H-<sup>15</sup>N HSQC spectra, corresponding to the Trp indole region, of (D) 280 μM Core in the presence of 190 mM DMPC/DHPC and (E) 520 μM Core<sup>L21A</sup> in the presence of 60 mM DMPC/DHPC, obtained at 38 °C. Resonances belonging to the post-fusion and lipid-bound states are labeled as ‘6HB’ and ‘L’, respectively. (F) Van’t Hoff analysis for the lipid-bound and 6HB equilibrium for Core (blue) and Core<sup>L21A</sup> (red).  $\Delta H$  and  $\Delta S$  were obtained from linear regression analysis. Energy differences are reported at 38 °C in units of kcal mol<sup>-1</sup> of a trimer. The changes in  $K_d$  with temperature are fully reversible, and values for Core were recorded by interleaving the temperature points at which data were recorded.

that bicelles are not stable entities; they rapidly fuse and dissociate. Once the transition barrier to monomerization has been crossed in the presence of two bicelles, the monomeric helices will rapidly and randomly distribute among the large excess of bicelles.

At 38 °C and 280 μM Core, the population of the lipid-bound state in the presence of 190 mM DMPC/DHPC (*i.e.*, 1.9 mM bicelle particles) is *ca* 34% (Figure 1(D)), corresponding to a dissociation constant ( $K_d$ ) of  $4.0 \times 10^{-3}$  (Eqs. (1)–(4)). The relatively low percentage of the lipid-bound state, even in the presence of a nearly seven-fold excess of bicelles, points to the high thermodynamic stability of Core.

To facilitate study of the dissociation kinetics, a single point mutation was introduced at the center

of the hydrophobic core of HR1 (L21A; termed Core<sup>L21A</sup>). Size exclusion chromatography in combination with multi-angle light scattering (SEC-MALS) revealed that the L21A mutation did not impact the oligomerization, as Core<sup>L21A</sup> retained its homotrimeric state (MW ~ 29 kDa, Figure 2 (C)). Moreover, a far-UV circular dichroism (CD) spectrum of Core<sup>L21A</sup> showed a typical  $\alpha$ -helical signature, albeit with a small, *ca.* 15%, reduction relative to the wild-type Core (Figure S3(A)). Thermodynamic stability of  $\alpha$ -helices is often evaluated by monitoring the CD signal at 222 nm ( $[\theta]_{222}$ ) with increasing temperatures, provided the protein folds reversibly (Figure S3(A)).<sup>20</sup> A 21 °C reduction in the melting temperature of Core<sup>L21A</sup> ( $T_m \sim 58$  °C; Figure S3(B)) relative to wild-type Core<sup>21,22</sup> points to its decreased stability, which is

also manifested by its increased population of the bicelle-bound state (Figure 2(E)). Even at a high (520  $\mu\text{M}$ ) concentration of Core<sup>L21A</sup> and a low (0.6 mM) concentration of DMPC/DHPC bicelles, the equilibrium has shifted towards the lipid-bound state ( $\sim 71\%$ , at protein:bicelle  $\approx 1:1.15$ ), corresponding to a  $K_d$  of 2.8 (Figure 2(E)).

The free-energy difference ( $\Delta G$ ) associated with the transition between the 6HB and lipid-bound conformations was obtained from Van't Hoff analysis. A linear fit of  $K_d$  against inverse temperature revealed a large enthalpy loss,  $\Delta H = -47.5 \text{ kcal mol}^{-1}$ , upon dissociation of Core, which we attribute to the disruption of HR1-HR1 and HR1-HR2 interactions in addition to weakening of hydrogen bonds (Figure 2(F)). However, dissociation of the compact 6HB structure into the more flexible, phospholipid-bound monomers resulted in a large change in entropy ( $T\Delta S = -44.1 \text{ kcal mol}^{-1}$  at 38 °C), nearly compensating for the large loss in enthalpy. Overall, the 6HB structure was found to be more stable than the bicelle-bound state by  $\Delta G \approx 3.4 \text{ kcal mol}^{-1}$  (per trimer) in the presence of 1.9 mM bicelles (Table 1). Inter-conversion between these two states is found to be reversible as exemplified by the change in populations when randomly varying the order of the temperature steps (Figure S1(C)–(E)). The small value of the free energy change ( $\Delta G \approx 0.6 \text{ kcal mol}^{-1}$ ) observed for Core<sup>L21A</sup> suggests that both states are about equally stable under comparable conditions (Figure 2(F)).

To analyze structural features of the lipid-bound monomeric state, we measured  $^{13}\text{C}'$  and  $^{13}\text{C}^\alpha$  chemical shifts. Deviations of  $^{13}\text{C}'$  and  $^{13}\text{C}^\alpha$  chemical shifts from random coil values ( $\Delta\delta^{13}\text{C}'$  and  $\Delta\delta^{13}\text{C}^\alpha$ )<sup>23</sup> are robust, residue-specific reporters on secondary structure.<sup>24</sup> Due to its lower stability compared to wild-type Core, chemical shifts of the monomeric lipid-bound state were obtained for Core<sup>L21A</sup>, thus minimizing overlap with the 6HB resonances. At 40 °C, we found that 200  $\mu\text{M}$  Core<sup>L21A</sup> in the presence of 200 mM DMPC/DHPC is strongly shifted to the bicelle-bound state (Figure S4). Fairly large, positive  $\Delta\delta^{13}\text{C}^\alpha$  and  $\Delta\delta^{13}\text{C}'$  secondary shifts were strong indicators of  $\alpha$ -helical structures for

both HR1 (residues N9-A33) and HR2 (residues D45-E60), whereas near-zero values for the linker (S35-G40) and C-terminal HR2 residues (Q63-K68) indicated a high degree of dynamic disorder for these regions (Figure 3(A)). The helical secondary structure we observed in the bicelle-bound state agrees well with that previously reported for fos-choline micelles.<sup>12</sup> For the bicelle-bound state, hydrogen exchange rates observed for the amides that are expected to be engaged in  $\alpha$ -helical H-bonds (residues R12-A33 and N49-E60) yielded relatively low protection factors, in the range of 5–100, indicating a substantial degree of dynamic disorder within the helical structures (Figure S5). Significantly lower NOE values, in the range of 0.5 to 0.65 for the bicelle-bound state, also pointed to substantial internal mobility in these  $\alpha$ -helical HR regions (Figure 3(C)). A similar degree of increased internal motions was reported for the lipid-bound HR1 domain of the SARS-CoV-2 fusion protein.<sup>17</sup> We note that, in the absence of lipids, Core<sup>L21A</sup> folds to a highly ordered 6HB structure, as judged by high  $^{15}\text{N}$ - $\{^1\text{H}\}$  heteronuclear NOE values (Figure 3(C)), similar to what was reported for wild-type Core.<sup>12</sup>

Exchange processes that are slow on the NMR chemical shift time scale ( $\lesssim 50 \text{ s}^{-1}$ ) but not much slower than the longitudinal relaxation rates (*ca.*  $1 \text{ s}^{-1}$ ) can be conveniently studied by ZZ-exchange experiments.<sup>25–27</sup> Exchange kinetics between the bicelle-bound and 6HB states of 520  $\mu\text{M}$  Core<sup>L21A</sup> were quantified at 38 °C, in the presence of 60 mM DMPC/DHPC. Representative regions of the  $^{15}\text{N}$  ZZ-exchange spectra, recorded at three mixing times (30 ms, 300 ms and 650 ms) show that for the shortest mixing time only the auto-correlation peaks for three Trp residues (W26, W41 and W44) are observed for both the 6HB and lipid-bound states (Figure 4(A)). Increasing the mixing times resulted in the appearance of new (red) cross-peaks that represent exchange between the two states (Figure 4(A)). Based on the intensity of these and other well-resolved backbone amide resonances, exchange rates were extracted by fitting the composite intensity ratio,  $\Xi(t)$ , to a quadratic function of the mixing time (Eq. (5)). Use of the composite intensity ratio is straightforward and effective, as this cancels out the effects of differences in  $R_1$

Table 1 Summary of thermodynamic properties associated with the gp41-Core equilibrium between lipid-bound and 6HB states.

	Enthalpy, $\Delta H$ (kcal mol <sup>-1</sup> )	Entropy, $T\Delta S$ (kcal mol <sup>-1</sup> )	Free energy, $\Delta G$ (kcal mol <sup>-1</sup> )
Dissociation (Activation, $k_{off}$ )	54.2 $\pm$ 3.6	41.3 $\pm$ 3.5	12.9 $\pm$ 1.1
Association (Activation, $k_{on}$ )	3.9 $\pm$ 1.9	-5.4 $\pm$ 1.8	9.3 $\pm$ 4.5
Dissociation (Equilibrium, $K_d$ )	47.5 $\pm$ 2.5	44.1 $\pm$ 1.0	3.4 $\pm$ 0.2

Gibbs free energies were calculated based on enthalpy and entropy ( $\Delta G = \Delta H - T\Delta S$ ) values at 38 °C.

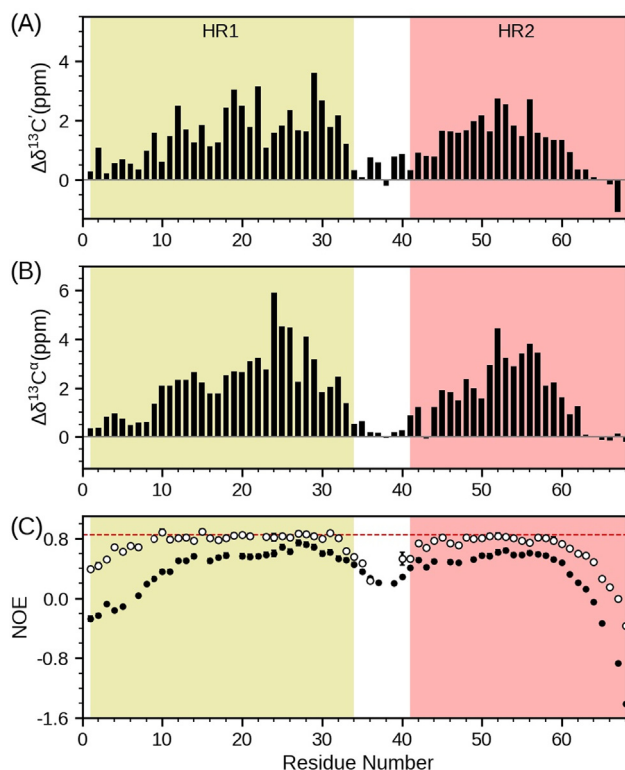


**Figure 3.** Secondary structure and flexibility of the lipid-bound state. Deviation of (A)  $^{13}\text{C}'$  and (B)  $^{13}\text{C}^\alpha$  chemical shifts of  $200\ \mu\text{M}\ [^{13}\text{C}/^{15}\text{N}]\text{-Core}^{\text{L21A}}$  from the neighbor-corrected random coil chemical shifts in the presence of  $200\ \text{mM}\ \text{DMPC/DHPC}$ . (C)  $^{15}\text{N}\text{-}\{^1\text{H}\}$  NOE (at  $600\ \text{MHz}$ ) of  $200\ \mu\text{M}\ [^{15}\text{N}/^2\text{H}]\text{-Core}^{\text{L21A}}$  in the presence (filled circles) and absence (open circles) of  $200\ \text{mM}\ \text{DMPC/DHPC}$ . The red dashed line displays the theoretical maximum NOE of  $0.85$  at  $600\ \text{MHz}$ . Regions corresponding to HR1 and HR2 are shown in light yellow and red background, respectively. Data collected at  $40\ ^\circ\text{C}$ .

(spin-lattice) relaxation rates between two distinct species.<sup>28,29</sup> Global fitting for six isolated resonances (backbone amides of S35, G37 and L54 and indole side chains of W21, W41 and W44) yielded a value for  $\zeta$  (*i.e.*,  $3k_{\text{on}}k_{\text{off}}[M]^2[B]^2$ ) of  $0.23 \pm 0.01\ \text{s}^{-2}$  (Figure 4(B)), whereas the extracted on- and off-rate constants (Equations 5–9) were  $k_{\text{on}} \approx 7.64 \times 10^5\ \text{M}^{-2}\ \text{s}^{-1}$  and  $k_{\text{off}} \approx 2.06 \times 10^6\ \text{M}^{-2}\ \text{s}^{-1}$ , respectively (Figure 4(C)). The overall exchange rate constant ( $k_{\text{ex}} = k_{\text{off}}[B]^2 + 3k_{\text{on}}[M]^2$ )<sup>30,31</sup> for this equilibrium was *ca*  $1.05\ \text{s}^{-1}$  at  $38\ ^\circ\text{C}$ , and a four-fold increase in  $k_{\text{ex}}$  ( $0.55$  to  $2.12\ \text{s}^{-1}$ ) was observed upon increasing the temperature from  $35$  to  $41\ ^\circ\text{C}$ .

For wild-type Core, exchange rates were found to be much slower than for Core<sup>L21A</sup>, as no cross-peaks could be observed in the ZZ-exchange spectrum even at mixing times as long as  $1100\ \text{ms}$  at  $38\ ^\circ\text{C}$ . To obtain measurable exchange rates, experiments were therefore repeated at higher temperatures, in the range of  $47$ – $52\ ^\circ\text{C}$ . A fit of the ZZ-exchange data obtained for  $280\ \mu\text{M}$  Core in the presence of  $190\ \text{mM}\ \text{DMPC/DHPC}$  yielded  $k_{\text{ex}} \approx 0.91\ \text{s}^{-1}$  at  $50\ ^\circ\text{C}$ , with  $k_{\text{on}}$  and  $k_{\text{off}}$  rate constants of  $2.68 \times 10^6\ \text{M}^{-2}\ \text{s}^{-1}$  and  $1.71 \times 10^5\ \text{M}^{-2}\ \text{s}^{-1}$ , respectively (Figure 4(D) and Figure S6). A

three-fold increase in  $k_{\text{ex}}$  from  $0.50$  to  $1.49\ \text{s}^{-1}$  was observed by increasing the temperature from  $47$  to  $52\ ^\circ\text{C}$ , and the extrapolated  $k_{\text{ex}}$  was found to be about  $8 \times 10^{-2}\ \text{s}^{-1}$  at  $38\ ^\circ\text{C}$ , *i.e.*, *ca.* 12 times slower than for Core<sup>L21A</sup>. However, a faster exchange rate for Core<sup>L21A</sup> does not imply faster membrane fusion. At  $200\ \text{mM}\ \text{DMPC/DHPC}$ , wild-type Core mostly adopts the 6HB state, whereas Core<sup>L21A</sup> predominantly samples the lipid-bound state (Figure 2(D), Figure 3, Figure S4), suggesting that Core<sup>L21A</sup> may not successfully mediate fusion. Indeed, earlier biochemical and *in vivo* infectivity assays showed that mutation of L21 (*i.e.*, L566 according to the full-length HXB2 gp160 numbering) in gp41 severely impacted viral infectivity, without altering its oligomeric state.<sup>32–35</sup>

Free-energy changes associated with the two states of wild-type Core were analyzed using the Eyring equation (Eq. (11))<sup>36</sup> by measuring rate constants at multiple temperatures. A caveat to this analysis is that, while enthalpy changes are readily obtained, the entropy contribution and overall free energy change depend on the assumed prefactor for the rate, which is likely to be much smaller in solution than the Eyring prefactor  $k_{\text{B}}T/h$ .<sup>37</sup> The dissociation activation parameters obtained from  $k_{\text{off}}$

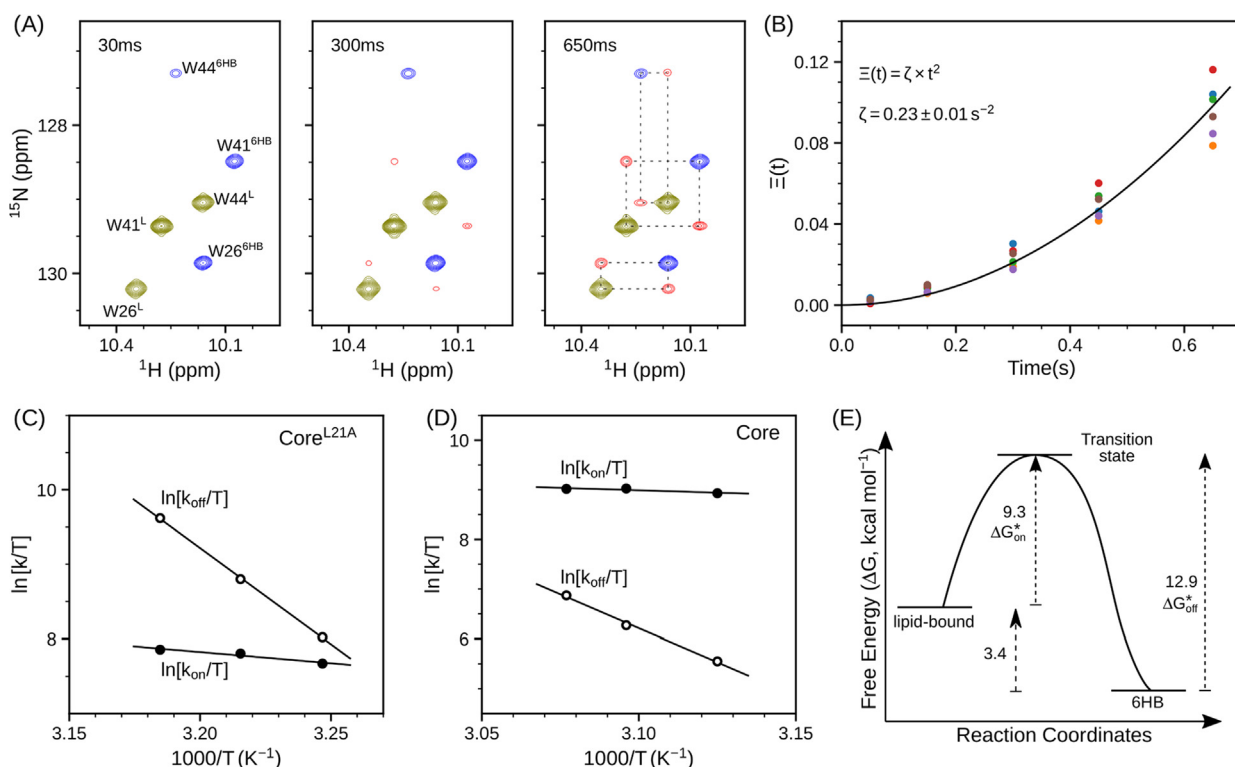


**Figure 4.** Slow exchange kinetics between lipid-bound and 6HB states. (A) Small regions from <sup>15</sup>N-ZZ HSQC spectra displaying Trp side chain indole resonances of Core<sup>L21A</sup> at 30, 300 and 650 ms mixing times at 38 °C. Auto-correlation resonances for the lipid-bound and 6HB states are shown in olive and blue, respectively, and cross-peaks observed at 300 ms and 650 ms are shown in red. (B) Plot of the composite intensity ratios,  $\Xi(t)$ , derived from six well-separated resonances (W21, S35, G37, W41, W44 and L54) resulted in a global fit of  $\zeta = 0.23 \text{ s}^{-2}$ . (C, D) Eyring plots showing the temperature dependence of  $k_{\text{on}}$  (filled circles) and  $k_{\text{off}}$  rates (open circles) for (C) Core<sup>L21A</sup> and (D) wild-type Core. (E) Free-energy diagram for the wild-type Core sequence, depicting the transition of the lipid-bound state to the lowest energy 6HB state through a high-energy transition state. Activation free energies are labeled with an asterisk (\*). Energy values are reported for 38 °C in units of kcal mol<sup>-1</sup>.

resulted in a  $\Delta G_{\text{off}}^*$  of 12.9 kcal mol<sup>-1</sup> (at 38 °C), which is significantly higher than the  $\Delta G$  (3.4 kcal mol<sup>-1</sup>) of the equilibrium obtained from  $K_{\text{d}}$  (Figure 4(E), Table 1). Further, a  $\Delta G_{\text{on}}^*$  of 9.3 kcal mol<sup>-1</sup> obtained from  $k_{\text{on}}$  suggests that the reaction pathway from the lipid-bound to the 6HB state proceeds through a high-energy transition state (Figure 4(E), Table 1). This transition state is dominated by a strong negative activation entropy ( $T\Delta S_{\text{on}}^* = -5.4 \text{ kcal mol}^{-1}$  at 38 °C) contribution, indicating that it is more ordered and compact than the bicelle-bound monomers. Prior stopped-flow CD measurements reported that the urea-denatured gp41-Core monomers transition through a high-energy state that resembles a fully native-like compact structure prior to formation of the 6HB.<sup>38</sup> Further, optical tweezer based single molecule kinetic studies on a similar gp41-Core construct reported a  $\Delta G$  of ca. 14 kcal mol<sup>-1</sup> (at 22 °C) between 6HB and 5HB states.<sup>39</sup> Here, 5HB differs from the 6HB state by the dissociation of one of the exterior HR2 helices. As the extrapolated  $\Delta G_{\text{off}}^*$  (15 kcal mol<sup>-1</sup> at 22 °C) between the transi-

tion state and 6HB in the current study is comparable to that observed with the optical tweezer method, it is plausible that the transition state probed in our work also resembles a relatively compact 5HB conformation.

Env-mediated membrane fusion is a relatively slow process with estimated times in the range of 10–30 minutes at 37 °C.<sup>40–43</sup> The current study, performed on a well-characterized minimal construct of the gp41 ectodomain, provides new insights into the energies and kinetics of the gp41 remodeling events from the intermediate lipid-bound to the final post-fusion state. An exchange time of ca. 12 seconds between these two states is much faster than the overall time scale of viral membrane fusion. However, prior to reaching the post-fusion state, hemifusion represents another obligatory intermediate step, where the apposed, proximal leaflets of the bilayers are merged while the distal leaflets remain intact (Figure 1(E)).<sup>44,45</sup> Because our experiments are conducted on a construct that lacks both the fusion peptide (FP) and the fusion peptide proximal region (FPPR) as well as

the membrane proximal external region (MPER) and the transmembrane (TM) helix, the hemifusion state is not accessible in our study. Moreover, because our study used isotropic bicelles, which can fuse edgewise and exhibit rapid lipid exchange during collisions in solution, the actual process of membrane fusion cannot be probed with our measurements. Structural studies in combination with molecular dynamic simulations reported associations between FP-FPPR and MPER-TM segments in the membrane environment, where a central three-helical bundle formed by FP is embraced by three TM helices in the post-fusion state.<sup>46,47</sup> Additionally, it appears plausible that *in vivo* the completion of 6HB formation takes place during or just after pore formation.<sup>48</sup> Nevertheless, it appears likely that the high energetic barrier associated with formation of the 6HB state, in addition to conformational arrangements associated with interactions between the FP-FPPR and MPER-TM segments during the transition from the hemi-fusion to the post-fusion state, contributes significantly to the remarkably slow time scale of membrane fusion between the HIV-1 virus and its host cell.

## Materials and Methods

### Recombinant protein expression and purification

The insert for the L21A variant of gp41-Core was synthesized and cloned into the pJ414 vector (ATUM). Both Core and Core<sup>L21A</sup> were expressed in *Escherichia coli* BL21 (DE3) and purified under denaturation conditions as described previously.<sup>12</sup> Reversed-phase high-performance liquid chromatography purified samples were folded in 50 mM sodium formate at pH 3, followed by 50 mM sodium acetate at pH 4, and finally against buffer A (20 mM sodium phosphate buffer at pH 6 containing 30 mM sodium chloride, 1 mM imidazole and 0.5 mM ethylenediaminetetraacetic acid). Isotope-enriched samples were prepared by growing the bacterial culture in M9/D<sub>2</sub>O medium supplemented with <sup>15</sup>N ammonium chloride and <sup>13</sup>C-d7 D-glucose or <sup>12</sup>C-d7 D-glucose as the sole nitrogen and carbon sources, respectively.

DMPC/DHPC phospholipid bicelles were prepared by dissolving DMPC powder into a DHPC solution. Total lipid ([DMPC] + [DHPC]) concentrations in the range of 60–200 mM were used in the study. The  $q$  value of the bicelles,  $\{[DMPC]/([DHPC] - [DHPC]_{free})\}$ , is maintained at 0.5, where  $[DHPC]_{free}$  is the monomer concentration ( $\sim 7$  mM) of DHPC that is in equilibrium between the bicelle and aqueous solution.<sup>49</sup> Unless stated otherwise, all bicelle and lipid concentrations refer to the total concentrations of lipid molecules.

### Backbone chemical shift assignments

Backbone chemical shift assignments were obtained for a 0.2 mM [<sup>13</sup>C/<sup>15</sup>N]-Core<sup>L21A</sup> sample in buffer A containing 200 mM DMPC/DHPC and 3% D<sub>2</sub>O. <sup>1</sup>H<sup>N</sup>, <sup>15</sup>N, <sup>13</sup>C <sup>$\alpha$</sup> , and <sup>13</sup>C' chemical shifts were obtained from TROSY-based HNCO and HNCA spectra recorded at 40 °C on a 700 MHz Bruker Avance-III spectrometer equipped with a triple axis gradient TXI cryogenic probe. Assignments were validated by inspection of a 3D <sup>1</sup>H<sup>N</sup>-<sup>15</sup>N-<sup>1</sup>H<sup>N</sup> NOESY-HMQC spectrum ( $\tau_{mix} = 150$  ms). Data were processed with NMRPipe<sup>50</sup> and analyzed using CCPNMR software.<sup>51</sup>

### Backbone relaxation experiments

<sup>15</sup>N-<sup>1</sup>H NOE measurements were made on a sample of 200  $\mu$ M [<sup>15</sup>N/<sup>2</sup>H]-Core<sup>L21A</sup> and collected in the absence and presence of 200 mM DMPC/DHPC, at pH 6 and 40 °C. Spectra were recorded at 600 MHz in an interleaved manner, where alternate free-induction decays were collected with and without 8 seconds of proton saturation.

### Monomer-Trimer dissociation equilibrium

The total concentration of protein was estimated based on absorbance at 280 nm ( $\epsilon = 17,990$  M<sup>-1</sup> cm<sup>-1</sup>). Unless specified otherwise, concentrations are reported for monomer units. The following monomer-trimer dissociation model is used for estimation of the coefficient of dissociation ( $K_d$ ).



$$K_d = \frac{[M]^3}{[T] \times [B]^2} \quad (2)$$

$$K_d = \frac{3[P_{tot}]^2 \times (a_M/a_T)^3}{(1 + a_M/a_T)^2 \times [B]^2} \quad (3)$$

$$[P_{tot}] = [M] + 3[T] \quad (4)$$

The free monomer ([M]) and trimer ([T]) concentrations at equilibrium were determined from the respective resonance amplitudes ( $a_M$  and  $a_T$ ) in a fully relaxed <sup>1</sup>H-<sup>15</sup>N HSQC spectrum, acquired using an interscan delay of seven seconds. The bicelle concentration, [B], was calculated by assuming that for  $q = 0.5$ , 100 lipids constitute a single bicelle particle (*i.e.*, 100 mM DMPC/DHPC  $\sim 1$  mM bicelle.<sup>52</sup> To minimize the impact of differences in transverse relaxation rates of 6HB and lipid-bound states on the amplitudes,  $K_d$  is reported as the average obtained for the two extreme C-terminal flexible residues (E67 & K68).

Thermodynamic properties, enthalpy ( $\Delta H$ ) and entropy ( $\Delta S$ ) differences between the trimer and monomer states were calculated as:

$$\ln(K_d) = \frac{\Delta H}{RT} - \frac{\Delta S}{R} \quad (5)$$

where R is the gas constant (0.00198 kcal mol<sup>-1</sup> K<sup>-1</sup>).

### <sup>15</sup>N ZZ exchange experiments

The NMR pulse sequence for <sup>15</sup>N ZZ exchange experiments is described elsewhere.<sup>27</sup> These experiments were collected for Core and Core<sup>L21A</sup> in the temperature range of 30 to 52 °C. To quantify the exchange rates, each experiment was recorded with 6 mixing times ranging from 30 to 1000 ms, using a pre-scan delay (d1) of 2 sec. The following equations were used to analyze resonance intensities in terms of  $K_d$ ,  $k_{on}$ ,  $k_{off}$ , and corresponding activation thermodynamic parameters:

$$\Xi(t) = \zeta t^2 \quad (6)$$

$$\zeta \approx k_{on}^{app} \times k_{off}^{app} \quad (7)$$

$$k_{on}^{app} = 3k_{on}[M]^2 \quad (8)$$

$$k_{off}^{app} = k_{off}[B]^2 \quad (9)$$

$$K_d = \frac{k_{off}}{k_{on}} \quad (10)$$

$$k_{ex} = k_{on}^{app} + k_{off}^{app} \quad (11)$$

$$\ln\left(\frac{k}{T}\right) = -\left(\frac{\Delta H}{RT}\right) + \ln\left(\frac{k_B}{h}\right) + \left(\frac{\Delta S}{R}\right) \quad (12)$$

where  $k$  is either  $k_{on}$  or  $k_{off}$ ,  $k_B$  is the Boltzmann constant and  $h$  is Planck's constant.

### Size exclusion chromatography-multiangle light scattering (SEC-MALS)

The molar mass of Core<sup>L21A</sup> was analyzed by analytical size exclusion chromatography with inline multi-angle light scattering (Wyatt-9250H2HC, DAWN Heleos; Wyatt Technology Inc.), refractive index and UV detectors. Samples (125  $\mu$ L) were applied to a pre-equilibrated Superdex-75 column (1.0  $\times$  30 cm) and eluted at a flow rate of 0.5 mL/min at room temperature in buffer A. The molar mass of Core<sup>L21A</sup> (29 kDa) was obtained using the Astra software provided with the instrument.

### Hydrogen exchange

Hydrogen exchange rates (HX) were obtained on 0.2 mM [<sup>15</sup>N/<sup>2</sup>H]-Core<sup>L21A</sup> in buffer A, containing 200 mM DMPC/DHPC, both at pH 6.1 and at pH 7. Rates were measured using the WEX-III TROSY experiment<sup>53</sup> with a recycle delay (d1) of 5 s over seven durations of the water inversion interval, ranging from 5 to 1000 ms. Measurements were carried out at 40 °C on a 700 MHz spectrometer. Intrinsic random coil HX rates were obtained from the SPHERE webserver.<sup>54</sup> pH values of the samples were derived from imidazole <sup>1</sup>H chemical shifts.<sup>55</sup>

### Circular Dichroism spectroscopy

Far-UV CD spectra were acquired on a JASCO J-810 spectropolarimeter using a 0.1-cm pathlength cuvette at 35 °C in buffer A. Measurements were performed with protein concentrations in the range of 15–30  $\mu$ M.

### Accession numbers

NMR backbone chemical shift assignments (<sup>1</sup>H, <sup>15</sup>N, <sup>13</sup>C and <sup>13</sup>C<sup>2</sup>) for Core<sup>L21A</sup> in the lipid-bound conformation have been deposited to the BMRB with accession code 51410 and provided as supplementary Table 1.

### CRedit authorship contribution statement

**Sai Chaitanya Chiliveri:** Conceptualization, Investigation, Writing – original draft. **John M. Louis:** Investigation. **Robert B. Best:** Conceptualization. **Ad Bax:** Conceptualization, Supervision.

### DECLARATION OF COMPETING INTEREST

The authors declare that they have no known competing financial interests or personal relationships that could have appeared to influence the work reported in this paper.

### Acknowledgements

We thank A. Aniana for help with protein expression and purification, J. L. Baber and J. Ying for technical support, and D. A. Torchia and G. M. Clore for valuable discussions. This work was supported by the Intramural Research Program of the National Institute of Diabetes and Digestive and Kidney Diseases (DK-075023).

### Appendix A. Supplementary data

Supplementary data to this article can be found online at <https://doi.org/10.1016/j.jmb.2022.167683>.

Received 23 April 2022;

Accepted 8 June 2022;

Available online 11 June 2022

### Keywords:

class I fusion protein;  
membrane fusion;  
fusion intermediate;  
slow-exchange kinetics;  
gp41 folding

### References

- Sodroski, J., Goh, W.C., Rosen, C., Campbell, K., Haseltine, W.A., (1986). Role of the HTLV-III/LAV envelope in syncytium formation and cytopathicity. *Nature* **322**, 470–474.
- Kowalski, M., Potz, J., Basiripour, L., Dorfman, T., Goh, W. C., Terwilliger, E., Dayton, A., Rosen, C., Haseltine, W., Sodroski, J., (1987). Functional regions of the envelope glycoprotein of human immunodeficiency virus type 1. *Science* **237**, 1351–1355.
- Eckert, D.M., Kim, P.S., (2001). Mechanisms of viral membrane fusion and its inhibition. *Annu. Rev. Biochem.* **70**, 777–810.
- Tamm, L.K., Lee, J., Liang, B., (2014). Capturing glimpses of an elusive HIV gp41 prehairpin fusion intermediate. *Structure* **22**, 1225–1226.
- Harrison, S.C., (2015). Viral membrane fusion. *Virology* **479–480**, 498–507.
- Rey, F.A., Lok, S.M., (2018). Common features of enveloped viruses and implications for immunogen design for next-generation vaccines. *Cell* **172**, 1319–1334.
- Chen, B., (2019). Molecular Mechanism of HIV-1 Entry. *Trends Microbiol.* **27**, 878–891.
- Chan, D.C., Fass, D., Berger, J.M., Kim, P.S., (1997). Core structure of gp41 from the HIV envelope glycoprotein. *Cell* **89**, 263–273.
- Tan, K., Liu, J.H., Wang, J.H., Shen, S., Lu, M., (1997). Atomic structure of a thermostable subdomain of HIV-1 gp41. *Proc. Natl. Acad. Sci. U. S. A.* **94**, 12303–12308.
- Ladinsky, M.S., Gnanapragasam, P.N.P., Yang, Z., West, A.P., Kay, M.S., Bjorkman, P.J., (2020). Electron tomography visualization of HIV-1 fusion with target cells

- using fusion inhibitors to trap the pre-hairpin intermediate. *Elife* **9**, e58411
- Ward, A.E., Kiessling, V., Pornillos, O., White, J.M., Ganser-Pornillos, B.K., Tamm, L.K., (2020). HIV-cell membrane fusion intermediates are restricted by Serinics as revealed by cryo-electron and TIRF microscopy. *J. Biol. Chem.* **295**, 15183–15195.
  - Roche, J., Louis, J.M., Grishaev, A., Ying, J., Bax, A., (2014). Dissociation of the trimeric gp41 ectodomain at the lipid–water interface suggests an active role in HIV-1 Env-mediated membrane fusion. *Proc. Natl. Acad. Sci. U. S. A.* **111**, 3425–3430.
  - Yu, Y.G., King, D.S., Shin, Y.K., (1994). Insertion of a coiled-coil peptide from influenza virus hemagglutinin into membranes. *Science* **266**, 274–276.
  - Sackett, K., Shai, Y., (2002). The HIV-1 gp41 N-terminal heptad repeat plays an essential role in membrane fusion. *Biochemistry* **41**, 4678–4685.
  - Korazim, O., Sackett, K., Shai, Y., (2006). Functional and structural characterization of HIV-1 gp41 ectodomain regions in phospholipid membranes suggests that the fusion-active conformation is extended. *J. Mol. Biol.* **364**, 1103–1117.
  - Aisenbrey, C., Bechinger, B., (2020). Structure, interactions and membrane topology of HIV gp41 ectodomain sequences. *Biochim. Biophys. Acta - Biomembr.* **1862**, 183274
  - Chiliveri, S.C., Louis, J.M., Ghirlando, R., Bax, A., (2021). Transient lipid-bound states of spike protein heptad repeats provide insights into SARS-CoV-2 membrane fusion. *Sci. Adv.* **7**, eabk2226.
  - Roche, J., Louis, J.M., Aniana, A., Ghirlando, R., Bax, A., (2015). Complete dissociation of the HIV-1 gp41 ectodomain and membrane proximal regions upon phospholipid binding. *J. Biomol. NMR* **61**, 235–248.
  - Sanders, C.R., Prosser, R.S., (1998). Bicelles: A model membrane system for all seasons? *Structure* **6**, 1227–1234.
  - Greenfield, N.J., (2006). Using circular dichroism collected as a function of temperature to determine the thermodynamics of protein unfolding and binding interactions. *Nat. Protoc.* **1**, 2527–2535.
  - Lu, M., Ji, H., Shen, S., (1999). Subdomain folding and biological activity of the Core structure from Human Immunodeficiency Virus type 1 gp41: Implications for viral membrane fusion. *J. Virol.* **73**, 4433–4438.
  - Louis, J.M., Baber, J.L., Clore, G.M., (2015). The C34 peptide fusion inhibitor binds to the six-helix bundle core domain of HIV-1 gp41 by displacement of the C-terminal helical repeat region. *Biochemistry* **54**, 6796–6805.
  - Kjaergaard, M., Brander, S., Poulsen, F.M., (2011). Random coil chemical shift for intrinsically disordered proteins: Effects of temperature and pH. *J. Biomol. NMR* **49**, 139–149.
  - Wang, Y., Jardetzky, O., (2002). Probability-based protein secondary structure identification using combined NMR chemical-shift data. *Protein Sci.* **11**, 852–861.
  - Montelione, G.T., Wagner, G., (1989). 2D Chemical exchange NMR spectroscopy by proton-detected heteronuclear correlation. *J. Am. Chem. Soc.* **111**, 3096–3098.
  - Wider, G., Neri, D., Wüthrich, K., (1991). Studies of slow conformational equilibria in macromolecules by exchange of heteronuclear longitudinal 2-spin-order in a 2D difference correlation experiment. *J. Biomol. NMR* **1**, 93–98.
  - Farrow, N.A., Zhang, O., Forman-Kay, J.D., Kay, L.E., (1994). A heteronuclear correlation experiment for simultaneous determination of  $^{15}\text{N}$  longitudinal decay and chemical exchange rates of systems in slow equilibrium. *J. Biomol. NMR* **4**, 727–734.
  - Miloushev, V.Z., Bahna, F., Ciatto, C., Ahlsen, G., Honig, B., Shapiro, L., Palmer, A.G., (2008). Dynamic properties of a type II Cadherin adhesive domain: Implications for the mechanism of strand-swapping of classical Cadherins. *Structure* **16**, 1195–1205.
  - Palmer, A.G., Koss, H., (2019). Chemical Exchange. *Methods Enzymol.* **615**, 177–236.
  - Palmer, A.G., Kroenke, C.D., Loria, J.P., (2001). Nuclear magnetic resonance methods for quantifying microsecond-to-millisecond motions in biological macromolecules, in. *Methods Enzymol.*, 204–238.
  - Rennella, E., Sekhar, A., Kay, L.E., (2017). Self-assembly of human Profilin-1 detected by Carr-Purcell-Meiboom-Gill Nuclear Magnetic Resonance (CPMG NMR) spectroscopy. *Biochemistry* **56**, 692–703.
  - Cao, J., Bergeron, L., Helseth, E., Thali, M., Repke, H., Sodroski, J., (1993). Effects of amino acid changes in the extracellular domain of the human immunodeficiency virus type 1 gp41 envelope glycoprotein. *J. Virol.* **67**, 2747–2755.
  - Chen, S.S., Lee, C.N., Lee, W.R., McIntosh, K., Lee, T.H., (1993). Mutational analysis of the leucine zipper-like motif of the human immunodeficiency virus type 1 envelope transmembrane glycoprotein. *J. Virol.* **67**, 3615–3619.
  - Pacheco, B., Alshafi, N., Debbeche, O., Prévost, J., Ding, S., Chappleau, J.-P., Herschhorn, A., Madani, N., Princiotto, A., Melillo, B., Gu, C., Zeng, X., Mao, Y., Smith, A.B., Sodroski, J., Finzi, A., (2017). Residues in the gp41 ectodomain regulate HIV-1 envelope glycoprotein conformational transitions induced by gp120-directed inhibitors. *J. Virol.* **91**, e02219–e2316.
  - Chen, S.-S.-L., Lee, S.-F., Hao, H.-J., Chuang, C.-K., (1998). Mutations in the leucine zipper-like heptad repeat sequence of Human Immunodeficiency Virus type 1 gp41 dominantly interfere with wild-type virus infectivity. *J. Virol.* **72**, 4765–4774.
  - Eyeing, H., (1935). The activated complex and the absolute rate of chemical reactions. *Chem. Rev.* **17**, 65–77.
  - Chung, H.S., Eaton, W.A., (2013). Single-molecule fluorescence probes dynamics of barrier crossing. *Nature* **502**, 685–688.
  - Marti, D.N., Bjelić, S., Lu, M., Bosshard, H.R., Jelesarov, I., (2004). Fast folding of the HIV-1 and SIV gp41 six-helix bundles. *J. Mol. Biol.* **336**, 1–8.
  - Jiao, J., Rebane, A.A., Ma, L., Gao, Y., Zhang, Y., (2015). Kinetically coupled folding of a single HIV-1 glycoprotein 41 complex in viral membrane fusion and inhibition. *Proc. Natl. Acad. Sci. U. S. A.* **112**, E2855–E2864.
  - Frey, S., Marsh, M., Günther, S., Pelchen-Matthews, A., Stephens, P., Ortlepp, S., Stegmann, T., (1995). Temperature dependence of cell-cell fusion induced by the envelope glycoprotein of human immunodeficiency virus type 1. *J. Virol.* **69**, 1462–1472.
  - Weiss, C.D., Barnett, S.W., Cacalano, N., Killeen, N., Littman, D.R., White, J.M., (1996). Studies of HIV-1 envelope glycoprotein-mediated fusion using a simple fluorescence assay. *AIDS* **10**, 241–246.

42. Muñoz-Barroso, I., Durell, S., Sakaguchi, K., Appella, E., Blumenthal, R., (1998). Dilution of the human immunodeficiency virus-1 envelope glycoprotein fusion pore revealed by the inhibitory action of a synthetic peptide from gp41. *J. Cell Biol.* **140**, 315–323.
43. Melikyan, G.B., Markosyan, R.M., Hemmati, H., Delmedico, M.K., Lambert, D.M., Cohen, F.S., (2000). Evidence that the transition of HIV-1 gp41 into a six-helix bundle, not the bundle configuration, induces membrane fusion. *J. Cell Biol.* **151**, 413–423.
44. Chernomordik, L.V., Kozlov, M.M., (2003). Protein-lipid interplay in fusion and fission of biological membranes. *Annu. Rev. Biochem.* **72**, 175–207.
45. Garg, H., Blumenthal, R., (2008). Role of HIV gp41 mediated fusion/hemifusion in bystander apoptosis. *Cell. Mol. Life Sci.* **65**, 3134.
46. Buzon, V., Natrajan, G., Schibli, D., Campelo, F., Kozlov, M.M., Weissenhorn, W., (2010). Crystal structure of HIV-1 gp41 including both fusion peptide and membrane proximal external regions. *PLoS Pathog.* **6**, e1000880
47. Caillat, C., Guilligay, D., Torralba, J., Friedrich, N., Nieva, J. L., Trkola, A., Chipot, C.J., Dehez, F.L., Weissenhorn, W., (2021). Structure of hiv-1 gp41 with its membrane anchors targeted by neutralizing antibodies. *Elife* **10**, e65005
48. Markosyan, R.M., Cohen, F.S., Melikyan, G.B., (2003). HIV-1 envelope proteins complete their folding into six-helix bundles immediately after fusion pore formation. *Mol. Biol. Cell* **14**, 926–938.
49. Chou, J.J., Baber, J.L., Bax, A., (2004). Characterization of phospholipid mixed micelles by translational diffusion. *J. Biomol. NMR* **29**, 299–308.
50. Delaglio, F., Grzesiek, S., Vuister, G.W., Zhu, G., Pfeifer, J., Bax, A., (1995). NMRPipe: A multidimensional spectral processing system based on UNIX pipes. *J. Biomol. NMR* **6**, 277–293.
51. Skinner, S.P., Fogh, R.H., Boucher, W., Ragan, T.J., Mureddu, Luca G., Vuister, W.G., (2016). CcpNmr AnalysisAssign: a flexible platform for integrated NMR analysis. *J. Biomol. NMR* **66**, 111–124.
52. Situ, A.J., Schmidt, T., Mazumder, P., Ulmer, T.S., (2014). Characterization of membrane protein interactions by isothermal titration calorimetry. *J. Mol. Biol.* **426**, 3670–3680.
53. Fitzkee, N.C., Torchia, D.A., Bax, A., (2011). Measuring rapid hydrogen exchange in the homodimeric 36 kDa HIV-1 integrase catalytic core domain. *Protein Sci.* **20**, 500–512.
54. Bai, Y., Milne, J.S., Mayne, L., Englander, S.W., (1993). Primary structure effects on peptide group hydrogen exchange. *Proteins Struct. Funct. Bioinforma.* **17**, 75–86.
55. Baryshnikova, O.K., Williams, T.C., Sykes, B.D., (2008). Internal pH indicators for biomolecular NMR. *J. Biomol. NMR* **41**, 5–7.